



MOF-derived 3D Fe-N-S co-doped carbon matrix/nanotube nanocomposites with advanced oxygen reduction activity and stability in both acidic and alkaline media

Huihui Jin^a, Huang Zhou^a, Daping He^{a,b,**}, Zhihao Wang^a, Qilei Wu^a, Qirui Liang^a, Suli Liu^{c,*}, Shichun Mu^{a,*}

^a State Key Laboratory of Advanced Technology for Materials Synthesis and Processing, Wuhan University of Technology, Wuhan, 430070, China

^b Hubei Engineering Research Center of RF-Microwave Technology and Application, Wuhan University of Technology, Wuhan, 430070, China

^c Key Laboratory of Advanced Functional Materials of Nanjing, Nanjing Xiaozhuang University, Nanjing, 21171, China

ARTICLE INFO

Keywords:

Carbon matrix
Carbon nanotubes
Composite
Oxygen reduction reaction
Zinc-air battery

ABSTRACT

MOF-derived carbon-based nanomaterials have attracted great attention due to the outstanding electrocatalytic performance, low-cost and super stability. To design an excellent catalyst, Fe, N and S codoped carbon matrix/carbon nanotube nanocomposites (Fe-N-S CNN) are prepared by pyrolysis of ZIF-8 impregnated with iron salt in this work. Benefiting from the synergistic effect of carbon matrix and nanotubes, abundant iron nitrides and thiophene-S active sites, the Fe-N-S CNN exhibits an excellent oxygen reduction reaction (ORR) performance with a half-wave potential of 0.91 V vs. RHE in alkaline conditions and 0.78 V vs. RHE in acidic conditions, while those of commercial Pt/C catalysts are 0.85 V vs. RHE and 0.795 V vs. RHE, respectively. Furthermore, Fe-N-S CNN as the cathode catalyst in a primary zinc-air battery shows a specific capacity of 700 mA h g⁻¹.

1. Introduction

In the past, oxygen reduction reaction (ORR) has seriously limited the development of efficient electrochemical devices (such as fuel cells, metal-air batteries, etc.) due to very sluggish reduction kinetics [1–5]. Although the Pt-based catalysts are the most effective catalysts for ORR and have been used in the commercialized fuel cell vehicles, the scarcity of Pt restricts large-scale applications [6–8]. Therefore, finding alternative catalysts with low-cost and high-efficiency is urgent for the widespread use of those electrochemical energy technologies. Carbon-based nanomaterials, especially carbons doped with heteroatoms (N, P, S, Fe, Co), have achieved outstanding catalytic activity (similar to or even better than Pt catalyst) and they have been considered as promising catalysts for ORR in the commercialization of electrochemical devices [9–13].

Carbon nanomaterials offer the combined advantages of high chemical stability, a good electrical conductivity and high surface area. Therefore, they have become one of the hot topics in energy materials and they have been widely used in lithium ion batteries, supercapacitors, electrocatalysts or as catalyst supports [14–20]. Recently,

Wang's group fabricated a 3D carbon electrocatalyst consisting of defect-enriched nanosheets and polyhedrons by an elegant carbonization method based on sealing NaCl into MOF materials [21]. The resulting non-Pt catalyst reveals a good ORR catalytic performance similar to Pt, and a highly promising discharge performance in zinc-air batteries. Among carbon nanomaterials, carbon nanotubes play a prominent role in electrocatalysis processes due to their unique tubular structure facilitating the transport of electrons and reactants [22–24]. Thiele's group reported a multi-heteroatom-doped defect-enriched carbon nanotubes based electrocatalyst, which reached a 0.81 V vs. RHE half-wave potential in alkaline ORR tests under rotating disk conditions. This catalyst can reach up to 70% performance compared to that of Pt as a cathode catalyst layer in an anion exchange membrane [25]. In addition, among all kinds of non-noble metal catalysts, heteroatomic Fe, N or S doping is prominent in ORR catalyst development. Recently, Xu and co-workers synthesized an atomically dispersed Fe/N-doped hierarchical carbon architectures that exhibited a slightly better ORR performance than Pt in alkaline conditions [26]. Zhang and co-workers used keratin to prepare S/N codoped graphene-like nanobubble and nanosheet hybrids, which exhibited a very promising ORR ability in

* Corresponding authors.

** Corresponding author at: State Key Laboratory of Advanced Technology for Materials Synthesis and Processing, Wuhan University of Technology, Wuhan, 430070, China.

E-mail addresses: hedaping@whut.edu.cn (D. He), niuniu_410@126.com (S. Liu), masc@whut.edu.cn (S. Mu).

<https://doi.org/10.1016/j.apcatb.2019.03.013>

Received 17 December 2018; Received in revised form 26 February 2019; Accepted 2 March 2019

Available online 06 March 2019

0926-3373/© 2019 Elsevier B.V. All rights reserved.

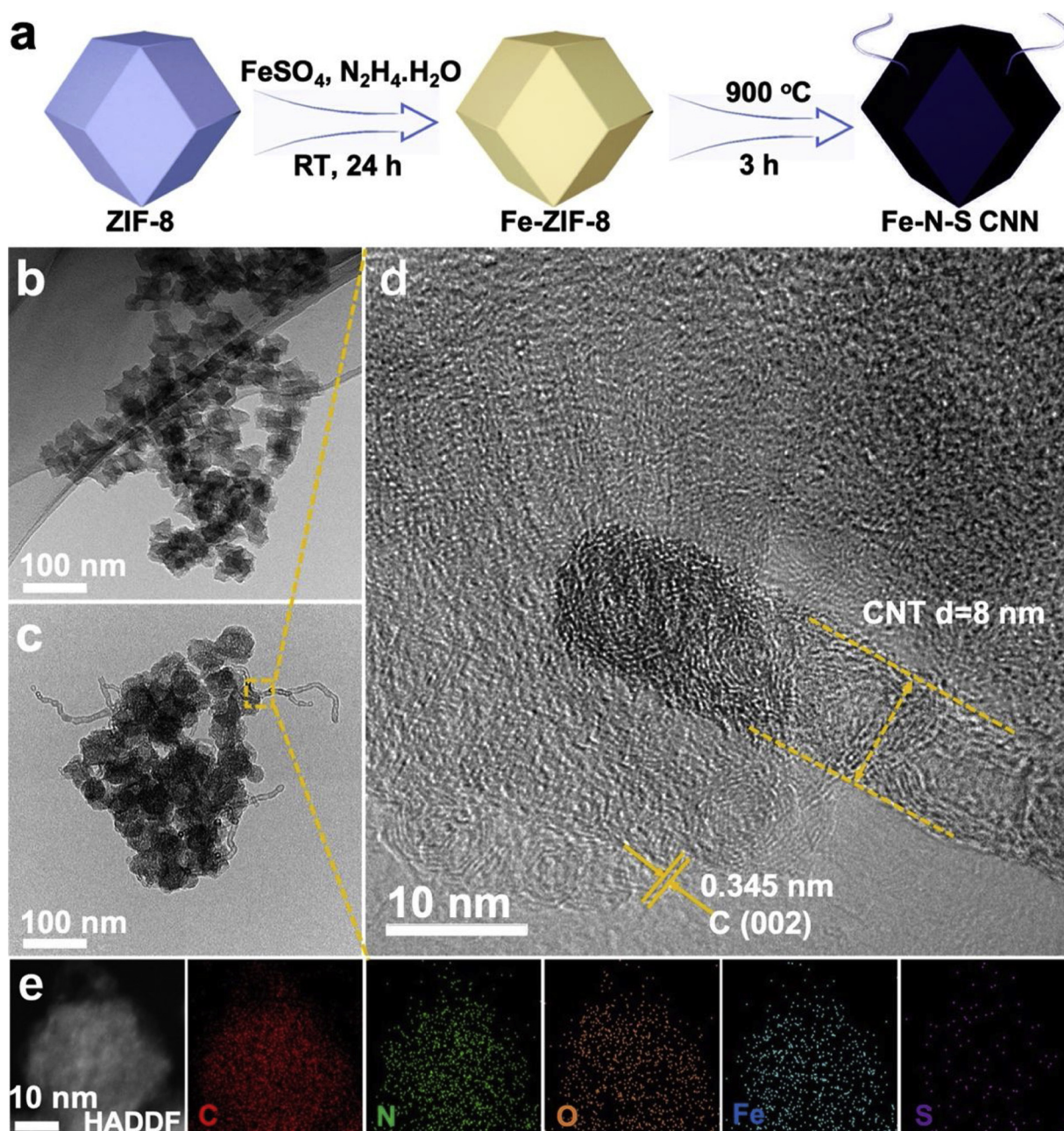


Fig. 1. (a) Schematic illustration of the synthetic process for Fe-N-S CNN; (b) TEM image of CN; (c) TEM image, (d) HRTEM image, (e) HAADF-STEM element mapping images of 6%Fe-N-S CNN.

alkaline conditions [27]. However, despite all those achievements, the ORR catalyst performance in both alkaline and acidic solutions still needs to be improved. New types of sustainable catalysts must be developed.

To further enhance the ORR performance of carbon-based nanomaterials, we designed a novel composite based on a carbon matrix with carbon nanotubes and doping with Fe, N, S atoms. It is known that metal-organic frameworks (MOF) precursors can be converted into a 3D carbon matrix with abundant N sites and transition metal sites after pyrolysis [28–30]. According to our previous work, the addition of Fe ions and hydrazine hydrate during the synthesis process of the MOF precursor could produce carbon nanotubes. Sulfur can be doped into the structure by inclusion of sulfate ions [31]. In addition, hydrazine hydrate, as an alkaline reductant, would not attack ZIF-8, and can therefore be employed to prevent the conversion of divalent iron into acidic trivalent iron which would damage the ZIF-8. However, the

direct addition of iron salt and hydrazine hydrate to the MOF precursor usually results in a complete destruction of the 3D framework structure. In this work, as shown in Fig. 1a, we use a facile and manageable impregnation method to prepare an effective combination of carbon matrix/nanotube 3D nanostructure. The first step is to impregnate ZIF-8 with ferrous sulfate solution and hydrazine hydrate, then the carbon matrix/nanotube nanocomposites doped with Fe, N and S (denoted as Fe-N-S CNN) are obtained by a further thermal pyrolysis processing. Compared with the commercial Pt/C catalyst, the as-prepared catalyst exhibits a much higher half-wave potential for oxygen reduction under alkaline reaction conditions and a comparable half-wave potential under acidic reaction conditions. The new catalyst also exhibits better stability in methanol solution, long working time durability, and excellent performance in primary zinc-air battery.

2. Experimental section

2.1. Electrocatalyst preparation

In this work, ZIF-8 was synthesized following the conventional synthetic method as reported previously in the literature [32]. Specifically, a methanol solution of zinc nitrate and 2-methylimidazole was stirred for 4 h at room temperature. Then, the white powder ZIF-8 (500 mg) was homogeneously dispersed in 50 mL methanol solution under ultrasonication for half an hour, and mixed with the solution of ferrous sulfate (10, 30, 60 mg, respectively) and hydrated hydrazine (10 mL) under stirring for another 24 h. After washing and drying, the precursor powders (named as x%Fe-ZIF-8, x represents iron with different amounts) were heat-treated at different temperatures (800, 900, 1000 °C) for different times (2, 3, 4 h) in an argon atmosphere. The products were named as x%Fe-N-S CNN. The carbide of ZIF-8 after pyrolysis was named as CN.

2.2. Materials characterization

Morphologies of as-synthesized products were obtained by scanning electron microscopy (SEM, Zeiss Ultra Plus) and by transmission electron microscopy (TEM, JEM-2100 F, 200 kV and Titan G2 60–300). Structures of as-synthesized samples were investigated by powder X-ray diffraction (PXRD, D/Max-RB at 12 kW using Cu K α radiation), by Raman spectroscopy (Renishaw Invia with an incident laser of 633 nm wavelength), by Fourier transform infrared spectroscopy (FTIR, Nicolet6700), and by X-ray photoelectron spectroscopy (XPS, ESCALAB 250Xi). Specific surface area was determined on an ASAP 2020 M at 77 K.

2.3. Electrochemical measurements

The electrochemical performance was measured on an AutoLab PG 302 N system under standard three-electrode measurement conditions. Rotating disk electrode (RDE) or rotating ring disk electrode (RRDE) measurements were performed with the working electrode coated with catalyst ink. A platinum wire and an Ag/AgCl electrode (filled with saturated potassium chloride) or a saturated calomel electrode (SCE) were used as the counter electrode and reference electrode, respectively. The Ag/AgCl electrode was used in alkaline solution, and SCE was used in acidic solution. The reference electrodes have been calibrated, and the potential for the Ag/AgCl electrode or the SCE have been converted to the reversible hydrogen electrode (RHE) scale using the Nernst equation. The working electrode was prepared as following: 5 mg catalyst was dispersed in a solution consisting of 900 μ L isopropanol, 100 μ L deionized water and 20 μ L Nafion (5%). The dispersion was sonicated to a homogeneous slurry. Then 20 μ L of such slurry was loaded on the glassy carbon of RDE and RRDE. Cyclic voltammetry (CV) experiments were performed in N₂/O₂ saturated aqueous 0.1 M KOH and aqueous 0.5 M H₂SO₄ without rotation, and Linear sweep voltammetry (LSV) was performed under 1600 rpm in O₂ saturated 0.1 M KOH and 0.5 M H₂SO₄ solutions. The scan speed was 10 mV s^{−1}.

2.4. Fabrication of home-made zinc-air batteries

2.4.1. Primary zinc-air battery

The primary zinc-air battery was based on a home-made electrochemical liquid battery. A catalyst-coated carbon paper (1 cm \times 1 cm) with a catalyst loading of 1.0 mg cm^{−2} and a zinc foil were used as the cathode and anode, respectively. The electrolyte was 6.0 M KOH and 0.2 M Zn(Ac)₂.

2.4.2. All solid-state zinc-air battery

The all solid-state zinc-air battery consists of a polished zinc foil as anode, nickel mesh loaded with catalysts as cathode, and a gel polymer

containing KOH and Zn(Ac)₂ as solid electrolyte. The gel polymer was prepared as follow: 0.297 g KOH, 0.165 g Zn(Ac)₂ and 1 g PVA powder were dispersed in 45 mL H₂O. The mixture was stirred into a transparent gel at 90 °C, then the gel was spread in a culture dish and frozen, followed by drying at 65 °C.

3. Results and discussion

3.1. Synthetic process and morphology analysis

Initially, the effects of adding hydrazine hydrate, of different pyrolysis temperatures (800, 900, 1000 °C) and of pyrolysis time (2, 3, 4 h) were explored. An optimized sample (based on electrochemical performance) was prepared by using hydrazine hydrate in the precursor and pyrolysis at 900 °C for 3 h. These initial experimental results are used for later discussion in this work (Fig. S1). The morphologies of the samples before and after pyrolysis are depicted in images obtained by scanning electron microscopy (SEM) and transmission electron microscopy (TEM). As shown in Fig. S2, Fe-ZIF-8 (ZIF-8 impregnated with different amounts of iron salt) maintains the angular octahedral structure with a size similar as that of virgin ZIF-8. This is then, converted into a composite of carbon matrix/nanotube 3D nanostructure after pyrolysis. The yield of carbon nanotubes increases with an increasing amount of iron salt (Fig. S3). In the TEM images (Fig. 1b, c), CN (derived from ZIF-8) perfectly keeps the polyhedral morphology, while carbon matrix and nanotubes can be clearly seen in 6%Fe-N-S CNN (derived from 500 mg ZIF-8 impregnated with 30 mg iron salts). Carbon nanotubes with 8 nm diameter are embedded in the carbon matrix (Fig. 1d), possibly resulting in a synergistic effect in the catalytic processes. Benefiting from the porous carbon matrix derived from ZIF-8, 6%Fe-N-S CNN shows a high surface area of 974 m² g^{−1} (Fig. S4). In addition, as shown in the HAADF-STEM mapping images (Fig. 1e), the C, N, O, Fe, and S elements are uniformly distributed on the carbon matrix/nanotube samples.

3.2. Structure analysis

Before pyrolysis, the diffraction peaks of Fe-ZIF-8 with different iron salt additions are consistent with ZIF-8, indicating that iron impregnation would not change the structure of ZIF-8 (Fig. 2a), which is also demonstrated by the Fourier-transform infrared spectra (Fig. S5). After pyrolysis, Fe-ZIF-8 was completely carbonized into an iron doped carbon-based material, and ICP results reveal that the Fe content indeed changed with different amounts of ferrous sulfate addition (Table S1). As shown in Fig. 2b, when the Fe content is low, there are only two carbon diffraction peaks corresponding to C(002) and C(100), respectively [33,34]. When the Fe content greatly increases, the peaks of iron oxides emerge, demonstrating that higher iron content leads to more iron oxides production in the pyrolysis process. In the Raman spectra (Fig. 2c), all carbonized samples exhibit two peaks indexed as D (1300 cm^{−1}) and G peak (1580 cm^{−1}), representing the defects of the C atom lattice and the in-plane stretching vibration of sp² bonded carbon atoms, respectively [35,36]. Compared with CN, the increased value of I_D/I_G in Fe-N-S CNN indicates that the addition of iron increases defects of the as-prepared samples. However, the value of I_D/I_G gradually decreases with the increase of iron content. This means that carbon atoms are more likely to be present in sp²-bonded form, suggesting that more carbon nanotubes can be produced as the iron content increases, which also can be verified by the SEM images in Fig. S3.

The binding situation of carbon can be divided into five peaks, C-sp², C-sp³, C–N, C–O and C=O, which correspond to the position of 284.5 eV, 285 eV, 286.2 eV, 286.6 eV and 288.1 eV, respectively [37,38]. Compared with CN, Fe-N-S CNN shows a pronounced C–N peak, suggesting that iron may promote the formation of C–N bonds (Fig. S6). The ratio of C-sp²/C-sp³ increases with the increase of the iron content (Fig. S7), which is consistent with the Raman results. However,

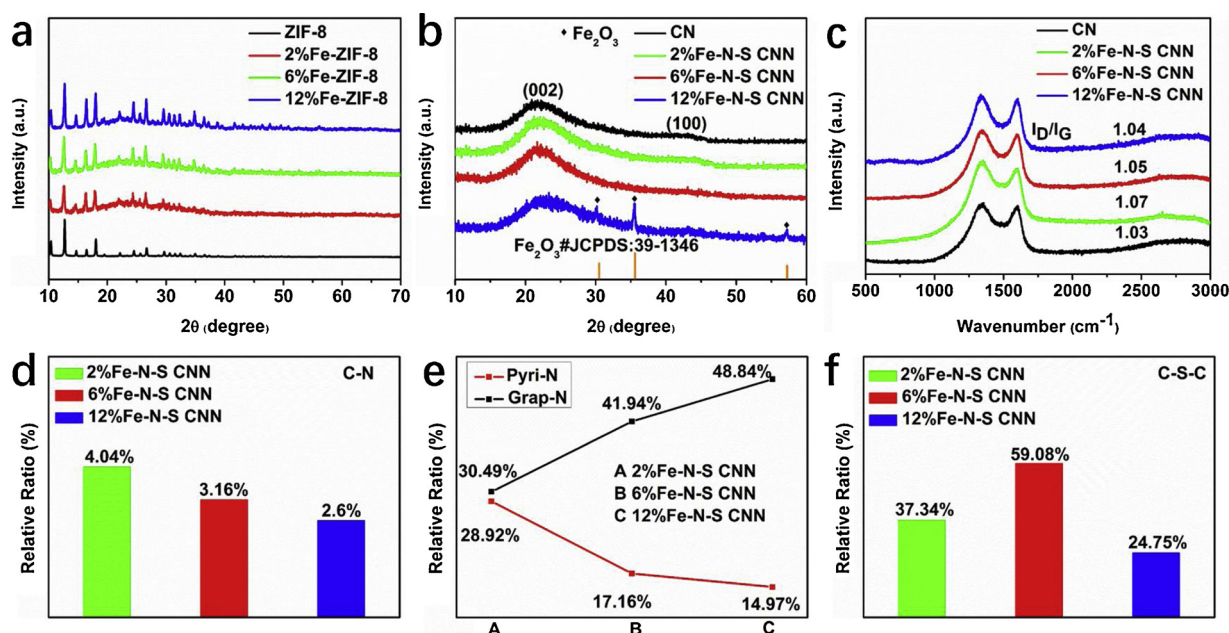


Fig. 2. XRD patterns of samples (a) before pyrolysis and (b) samples after pyrolysis; (c) Raman spectra of the samples after pyrolysis; (d) C-N content, (e) Pyri-N and Grap-N content, (f) C-S-C content in the pyrolysis samples in different catalysts from XPS results.

as seen from Fig. 2d, the more iron in the product, the less content of C-N bonds, due to the selective cleavage of C-N bond near Fe-Nx, where the C-N cleavage would expose the active sites Fe-Nx to improve the ORR performance [39]. The high-resolution N 1s spectrum can be fitted into three peaks at 398.2 eV, 400.1 eV and 401.1 eV, corresponding to pyridinic N (pyri-N), pyrrolic N (pyrr-N), and graphitic N (grap-N), respectively (Fig. S8) [40,41]. Pyri-N bonds to two carbon atoms and one sp^2 orbital of N is occupied by a pair of lone electrons, which can increase the electron donor of carbon materials to improve the oxygen adsorption capacity and the onset potential [42,43]. Grap-N bonds to three carbon atoms with a lone electron left that can effectively attenuate the oxygen-oxygen bond and accelerate the oxygen reduction reaction, resulting in an enhancement of the limiting current density and electron transfer number for ORR [44,45]. Fig. 2e shows the content changes of pyri-N and grap-N in different products. With the increase of iron content, the changes of pyri-N and grap-N are completely opposite. The increase in grap-N content is due to the increase of carbon nanotubes, while the decrease in pyri-N content is attributed to the fact that the bonds of pyri-N and carbon are the main source of C-N selective cleavage [39]. Therefore, according to the analysis of Fig. 2d, e, 6%Fe-N-S CNN has more exposed Fe-Nx sites and grap-N than 2%Fe-N-S CNN, and more pyri-N than 12%Fe-N-S CNN. In addition, since the catalytic reaction usually occurs preferentially on the surface of the products, the content of surface N and surface Fe would affect the ORR performance. Table S1 gives the contents of surface N and Fe in different samples. The surface N atomic percentage in 6%Fe-N-S CNN (9.65%) is close to 2%Fe-N-S CNN (10.07%), higher than 12%Fe-N-S CNN (8.2%), and the surface Fe atomic percentage in 6%Fe-N-S CNN (1.6%) is very close to 12%Fe-N-S CNN (1.68%), much higher than 2%Fe-N-S CNN (1.37%). Meanwhile, iron oxides on the surface of 12%Fe-N-S CNN could cover some active sites. Therefore, 6% Fe-N-S CNN has the most exposed Fe-Nx active sites for ORR. In terms of the doping with S, based on the Fourier-transform infrared spectra (Fig. S5), the adsorbed SO_4^{2-} ions on Fe-ZIF-8 were completely decomposed after high temperature pyrolysis. Fig. S9 shows evidence for the formation of doped S in the as-prepared products. The S2p peak can be fitted into thiophene-S (C-S-C, 163.9 eV and 165 eV) and oxidized-S (SOx-C, 167.8 eV) [46,47]. Thiophene-S has been proved to change charge spin density and collaborate with doped N to promote ORR activity [48]. The thiophene-S percent and surface S atomic percentage

in each sample are displayed in Fig. 2f and Table S1. Compared with 2% Fe-N-S CNN and 12% Fe-N-S CNN, 6%Fe-N-S CNN has the highest content of thiophene-S. Fe2p spectra show that both Fe^{2+} and Fe^{3+} exist in all the samples (Fig. S10), and more Fe^{3+} was generated in the sample with high iron content (Fig. S11), which matches the XRD results well.

3.3. Electrocatalytic performance

The electrochemical investigation of ORR performance of Fe-N-S CNN catalyst materials was based on three electrode measurements under rotating disk conditions. In O_2 -saturated 0.1 M KOH solution, data from linear sweep voltammetry (LSV) shows that 6%Fe-N-S CNN has a high half-wave potential ($E_{1/2}$) of 0.91 V vs. RHE, much better than commercial Pt/C ($E_{1/2}$ = 0.85 V vs. RHE) (Fig. 3a), showing a superior ability for catalyzing the ORR process. To further reveal the ORR process kinetics, four-electron selectivity measurements were performed using a rotating ring disk electrode (RRDE). Data from these measurements show that 6%Fe-N-S CNN has a much lower ring current (0.0014 mA) than that of commercial Pt/C (0.005 mA), which makes it clear that the new nanocomposites have stronger activities for oxygen reduction and peroxide reduction (Fig. 3b). More quantitatively, the H_2O_2 yield is below 2%, and the electron transfer number (n) is ~ 4 on the basis of RRDE data and Koutecky-Levich (K-L) plots (Fig. S12, 13). This indicates that the ORR process catalyzed by 6%Fe-N-S CNN is essentially a pure four-electron process. Furthermore, the calculated Tafel plots in Fig. S14 also show that 6%Fe-N-S CNN exhibits the fastest kinetics. For considering the practicability of cathode catalysts, the durability and methanol tolerance need to be tested. Current-time chronoamperometric responses were recorded for 6%Fe-N-S CNN and for commercial Pt/C at a rotation speed of 1600 rpm. Fig. 3c shows that methanol has no obvious toxic effect on 6%Fe-N-S CNN. In the durability test, the current loss of 6%Fe-N-S CNN is just 5.21% after operation for 12 h, while the current of commercial Pt/C decreases by 29.05% only after 4 h (Fig. 3d). After durability tests, 6%Fe-N-S CNN only shows 3 mV negative shift of half-wave potential, which is much smaller than 25 mV negative shift observed for the commercial Pt/C (Fig. S15). These results clearly demonstrate that 6%Fe-N-S CNN has superior durability in alkaline medium, even with methanol addition.

To better understand the active sites of 6%Fe-N-S CNN, acid etching

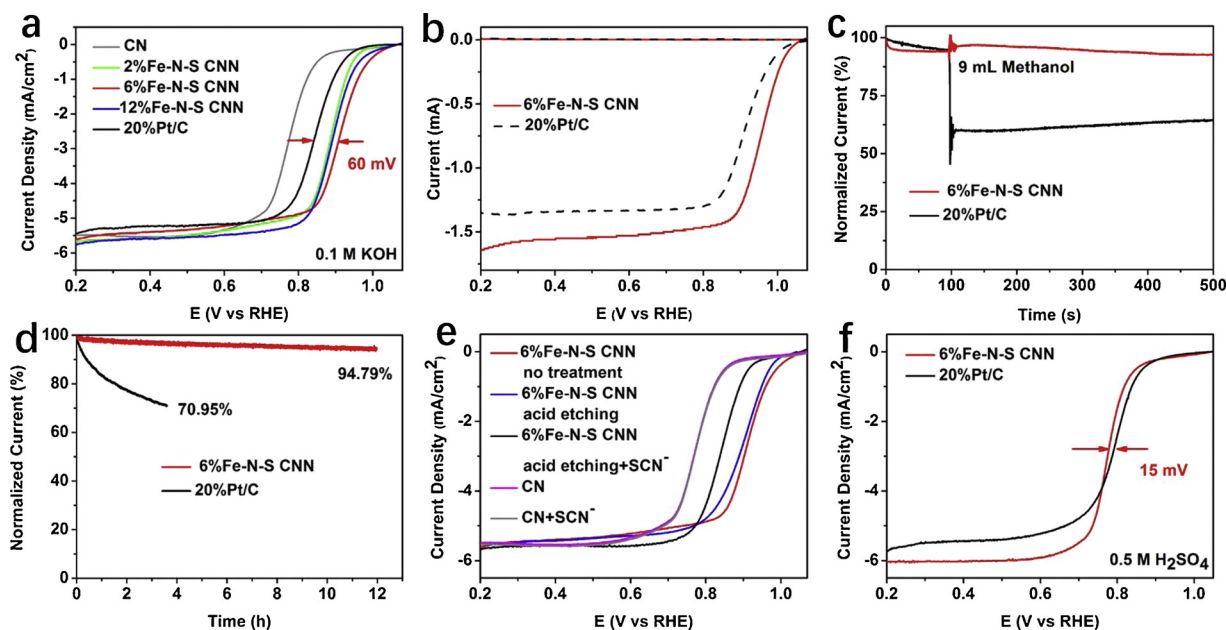


Fig. 3. (a) ORR polarization curves of different catalysts in O_2 saturated 0.1 M KOH electrolyte; (b) RRDE test, (c) Methanol tolerance test, (d) Durability test for 6% Fe-N-S CNN and 20%Pt/C; (e) before and after acid etching and SCN^- poison for 6%Fe-N-S CNN and CN; (f) ORR polarization curves of 6%Fe-N-S CNN and 20%Pt/C in O_2 saturated 0.5 M H_2SO_4 electrolyte.

and SCN^- poisoning experiments were carried out (Fig. 3e). With acid etching on 6%Fe-N-S CNN, the half-wave potential decreases slightly, indicating that some acid soluble substances on the surface of 6%Fe-N-S CNN have a positive effect on promoting the ORR activity. Furthermore, using 0.01 M KSCN to poison CN and 6%Fe-N-S CNN, the half-wave potential of 6%Fe-N-S CNN drops rapidly, while CN remains unchanged, demonstrating that Fe-Nx sites poisoned by SCN^- are the main ORR active sites in 6%Fe-N-S CNN.

In O_2 -saturated 0.5 M H_2SO_4 solution, 6%Fe-N-S CNN shows a comparable ORR activity to commercial Pt/C. LSV plots show that the half-wave potential of 6%Fe-N-S CNN is 0.78 V vs. RHE, which is almost the same as that for commercial Pt/C ($E_{1/2} = 0.795$ V vs. RHE) (Fig. 3f). H_2O_2 yields are calculated to be below 1% in the range of 0.2–0.9 V, and n is calculated to be ~ 4 based on the RRDE measurements and K-L plots (Fig. S16, 17). Both indicate that the ORR process is still an efficient four-electron path in acidic medium. In comparison with commercial Pt/C, 6%Fe-N-S CNN still keeps its excellent durability and methanol tolerance in acidic media (Fig. S18, 19). These results show that 6%Fe-N-S CNN has an excellent performance, and is superior to most reported non-noble metal ORR catalysts (Table S2). This catalyst even can be effective as a potential candidate as an ORR catalyst to replace commercial Pt/C.

3.4. Zinc-air battery performance

In view of the outstanding ORR performance of the 6%Fe-N-S CNN catalyst, it was further used as cathode in home-made zinc-air batteries. The polarization and power density curves show that 6%Fe-N-S CNN can deliver a much higher peak power density of 132 mW cm^{-2} compared to that for commercial Pt/C (73 mW cm^{-2}) (Fig. 4a). When 6%Fe-N-S CNN is used in all-solid-state zinc-air battery as shown in Fig. 4b, the open-circuit voltage can reach 1.37 V, and three connected batteries can lighten a ~ 3.5 V commercial light bulb (Fig. 4c). In addition, 6%Fe-N-S CNN displays better stability than commercial Pt/C in long time galvanostatic discharge testing under currents of 5 mA and 20 mA. This catalyst always produces higher voltages than those produced by commercial Pt/C catalyst (Fig. 4d, e). This battery has a high specific capacity of 700 mA h g^{-1} ($\approx 85.4\%$ of theoretical capacity of 820 mA h g^{-1}) based on the mass of zinc consumed for complete discharge at

20 mA cm^{-2} (Fig. S20). Moreover, when 6%Fe-N-S CNN experienced discharge under different current density and for a high current density ($2, 5, 10, 20, 50 \text{ mA cm}^{-2}$), followed by discharge at 2 mA cm^{-2} , the output voltage can remain the same as before, revealing that 6%Fe-N-S CNN has excellent and stable discharge performance (Fig. 4f). The superior zinc-air battery performance can be attributed to the efficient ORR activity and stability of 6%Fe-N-S CNN. These results demonstrate that 6%Fe-N-S CNN may be competitive in various related electrochemical devices.

4. Conclusions

In summary, we have successfully prepared a composite consisting of a 3D carbon matrix and carbon nanotubes doped with Fe, N and S (Fe-N-S CNN). The carbon matrix derived from ZIF-8 provides a high surface area and abundant nitrogen sites. The in situ formed carbon nanotubes not only increase the conductivity of the catalyst but also provide plentiful electron and reactant transport channels. With the synergistic effects of high surface area, good conductivity, abundant Fe-Nx, C-S-C active sites, and transport channels, this nanocomposite exhibits outstanding electrocatalytic activity for ORR processes with a high half-wave potential, excellent stability and good tolerance to methanol. Furthermore, Fe-N-S CNN when acting as the cathode in the primary zinc-air battery also shows an excellent and stable performance. This innovative development provides a new way to design a much wider variety of high performance and multifunctional materials.

Acknowledgements

This work was supported by the National Natural Science Foundation of China (51701146, 51672204). We thank Prof. Frank Marken from University of Bath for language editor and for helpful discussion.

Appendix A. Supplementary data

Supplementary material related to this article can be found, in the online version, at doi:<https://doi.org/10.1016/j.apcatb.2019.03.013>.

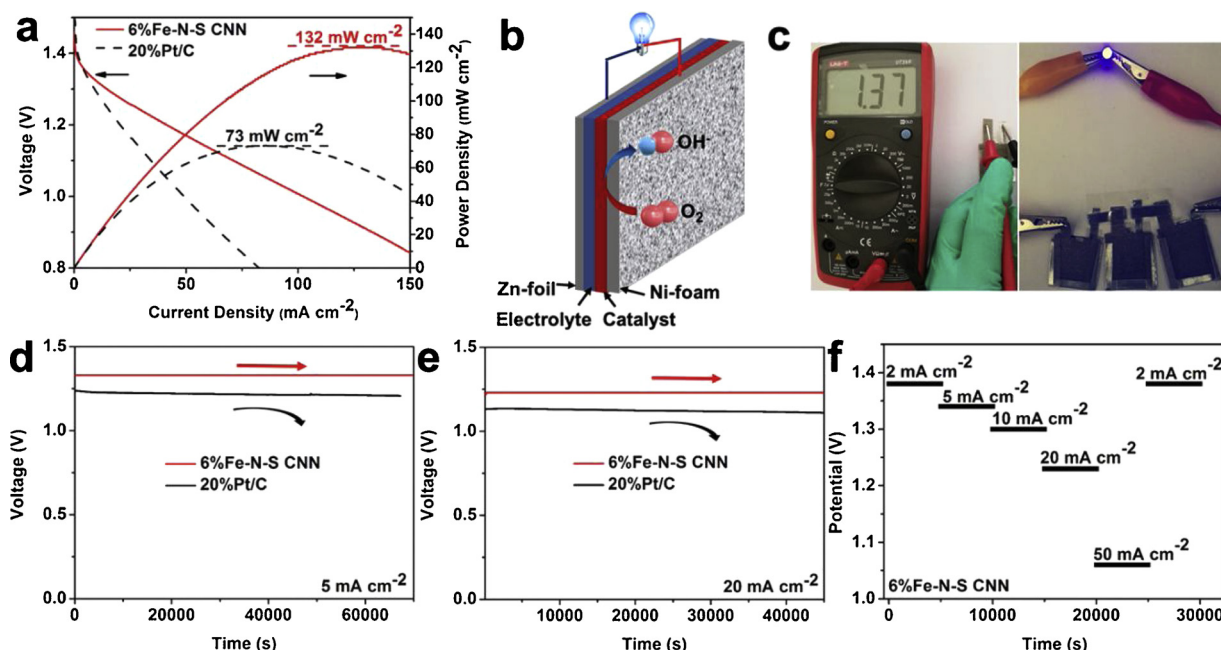


Fig. 4. (a) Polarization and power density curves of 6%Fe-N-S CNN and 20%Pt/C; (b) schematic diagram of the all-solid-state zinc-air battery; (c) Photographs of the open-circuit voltage and a lighted lamplet powered by three all-solid-state zinc-air batteries with using 6%Fe-N-S CNN as the cathode; (d) 5 mA cm⁻² discharge, (e) 20 mA cm⁻² discharge of 6%Fe-N-S CNN and 20%Pt/C; (f) Different current density discharge of 6%Fe-N-S CNN.

References

- J. Shen, Z. Tu, S. Chan, Enhancement of mass transfer in a proton exchange membrane fuel cell with blockage in the flow channel, *Appl. Therm. Eng.* 149 (2019) 1408–1418.
- H. Chang, C. Duan, X. Xu, H. Pei, S. Shu, Z. Tu, Technical performance analysis of a micro-combined cooling, heating and power system based on solar energy and high temperature PEMFC, *Int. J. Hydrogen. Energy* (2019), <https://doi.org/10.1016/j.ijhydene.2018.11.217>.
- C. Choi, M. Chung, H. Kwon, S. Parka, S. Woo, B. N- and P, N-doped graphene as highly active catalysts for oxygen reduction reactions in acidic media, *J. Mater. Chem. A* 1 (2013) 3694–3699.
- A. Zitolo, V. Goellner, V. Armel, M. Sougrati, T. Mineva, L. Stievano, E. Fonda, F. Jaouen, Identification of catalytic sites for oxygen reduction in Iron- and nitrogen-doped graphene materials, *Nat. Mater.* 14 (2015) 937–942.
- J. Wang, Z. Huang, W. Liu, C. Chang, H. Tang, Z. Li, W. Chen, C. Jia, T. Yao, S. Wei, Y. Wu, Y. Li, Design of N-Coordinated dual-metal sites: a stable and active Pt-free catalyst for acidic ORR, *J. Am. Chem. Soc.* 139 (2017) 17281–17284.
- Z. Yang, I. Moriguchi, N. Nakashima, Durable Pt electrocatalyst supported on a 3D nanoporous carbon shows high performance in a high-temperature polymer electrolyte fuel cell, *ACS Appl. Mater. Interfaces* 7 (2015) 9800–9806.
- Y. Nie, L. Li, Z. Wei, Recent advancements in Pt and Pt-free catalysts for oxygen reduction reaction, *Chem. Soc. Rev.* 44 (2015) 2168–2201.
- J. Dombrowski, A. Palmqvist, Recent progress in synthesis, characterization and evaluation of non-precious metal catalysts for the oxygen reduction reaction, *Fuel Cells* 16 (2016) 14–22.
- J. Wang, G. Han, L. Wang, L. Du, G. Chen, Y. Gao, Y. Ma, C. Du, X. Cheng, P. Zuo, G. Yin, ZIF-8 with ferrocene encapsulated: a promising precursor to single-atom Fe embedded nitrogen-doped carbon as highly efficient catalyst for oxygen electro-reduction, *Small* 14 (2018) 1704282.
- M. Wu, E. Zhang, Q. Guo, Y. Wang, J. Qiao, K. Li, P. Pei, N/S-Me (Fe, Co, Ni) doped hierarchical porous carbons for fuel cell oxygen reduction reaction with high catalytic activity and long-term stability, *Appl. Energy* 175 (2016) 468–478.
- T. Palaniselvam, V. Kashyap, S. Bhande, J. Baek, S. Kurungot, Nanoporous graphene enriched with Fe/Co-N active sites as a promising oxygen reduction electrocatalyst for anion exchange membrane fuel cells, *Adv. Funct. Mater.* 26 (2016) 2150–2162.
- Y. Wang, Y. Lai, L. Song, Z. Zhou, J. Liu, Q. Wang, X. Yang, C. Chen, W. Shi, Y. Zheng, M. Rauf, S. Sun, S-doping of an Fe/N/C ORR catalyst for polymer electrolyte membrane fuel cells with high power density, *Angew. Chem. Int. Ed* 54 (2015) 9907–9910.
- S. Zhao, J. Liu, C. Li, W. Ji, M. Yang, H. Huang, Y. Liu, Z. Kang, Tunable ternary (N, P, B)-doped porous nanocarbons and their catalytic properties for oxygen reduction reaction, *ACS Appl. Mater. Inter.* 6 (2014) 22297–22304.
- B. You, N. Jiang, M. Sheng, W. Drisdell, J. Yano, Y. Sun, Bimetal-organic framework self-adjusted synthesis of support-free nonprecious electrocatalysts for efficient oxygen reduction, *ACS Catal.* 5 (2015) 7068–7076.
- X. Ma, X. Zhao, J. Huang, L. Sun, Q. Li, X. Yang, Fine Co nanoparticles encapsulated in a N-Doped porous carbon matrix with superficial N-Doped porous carbon nanofibers for efficient oxygen reduction, *ACS Appl. Mater. Inter.* 9 (2017) 21747–21755.
- M. Xiao, J. Zhu, L. Ma, Z. Jin, J. Ge, X. Deng, Y. Hou, Q. He, J. Li, Q. Jia, S. Mukerjee, R. Yang, Z. Jiang, D. Su, C. Liu, W. Xing, Microporous framework induced synthesis of single-atom dispersed Fe-N-C acidic ORR catalyst and its in situ reduced Fe-N₄ active site identification revealed by X-ray absorption spectroscopy, *ACS Catal.* 8 (2018) 2824–2832.
- Z. Kou, L. Zhang, Y. Ma, X. Liu, W. Zang, J. Zhang, S. Huang, Y. Du, K. Cheenham, J. Wang, 2D carbide nanomeshes and their assembling into 3D microflowers for efficient water splitting, *Appl. Catal. B Environ.* 243 (2019) 678–685.
- Y. Ma, A. Sumboja, W. Zang, S. Yin, S. Wang, J. Pennycook, Z. Kou, Z. Liu, X. Li, J. Wang, Flexible and wearable all-solid-state Al-Air battery based on iron carbide encapsulated in electrospun porous carbon nanofibers, *ACS Appl. Mater. Inter.* 11 (2019) 1988–1995.
- S. Liu, Z. Wang, S. Zhou, F. Yu, M. Yu, C. Chiang, W. Zhou, J. Zhao, J. Qiu, Metal-organic-Framework-Derived hybrid carbon nanocages as a bifunctional electrocatalyst for oxygen reduction and evolution, *Adv. Mater.* 29 (2017) 1700874.
- B. Xia, Y. Yan, N. Li, H. Wu, X. Lou, X. Wang, A metal-organic framework-derived bifunctional oxygen electrocatalyst, *Nat. Energy* 1 (2016) 15006.
- Y. Wang, L. Tao, Z. Xiao, R. Chen, Z. Jiang, S. Wang, 3D carbon electrocatalysts in situ constructed by Defect-Rich Nanosheets and polyhedrons from NaCl-Sealed zeolitic imidazolate frameworks, *Adv. Funct. Mater.* 28 (2018) 1705356.
- L. Yang, S. Jiang, Y. Zhao, L. Zhu, S. Chen, X. Wang, Q. Wu, J. Ma, Y. Ma, Z. Hu, Boron-doped carbon nanotubes as metal-free electrocatalysts for the oxygen reduction reaction, *Angew. Chem. Int. Ed* 123 (2011) 7270–7273.
- C. Zhu, S. Fu, J. Song, Q. Shi, D. Su, M. Engelhard, X. Li, D. Xiao, D. Li, L. Estevez, D. Zhu, Y. Lin, Self-assembled Fe-N-Doped carbon nanotube aerogels with single-atom catalyst feature as high-efficiency oxygen reduction electrocatalysts, *Small* 13 (2017) 1603407.
- N. Andersen, A. Serov, P. Atanassov, Metal Oxides/CNT nano-composite catalysts for oxygen Reduction/Oxygen evolution in alkaline media, *Appl. Catal. B Environ.* 163 (2015) 623–627.
- C. Pham, B. Britton, T. Böhm, S. Holdcroft, S. Thiele, Doped, defect-enriched carbon nanotubes as an efficient oxygen reduction catalyst for anion exchange membrane fuel cells, *Adv. Mater. Interfaces* 5 (2018) 1800184.
- Q. Zhu, W. Xia, L. Zheng, R. Zou, Z. Liu, Q. Xu, Atomically dispersed Fe/N-Doped hierarchical carbon architectures derived from a metal-organic framework composite for extremely efficient electrocatalysis, *ACS Energy Lett.* 2 (2017) 504–511.
- J. Zhang, H. Zhou, X. Liu, J. Zhang, T. Peng, J. Yang, Y. Huang, S. Mu, Keratin-derived S/N Co-doped graphene-like nanobubble and nanosheet hybrids for highly efficient oxygen reduction, *J. Mater. Chem. A* 4 (2016) 15870–15879.
- B. Guan, Y. Lu, Y. Wang, M. Wu, X. Lou, Iron-cobalt Alloy/Nitrogen-Doped carbon cages synthesized via pyrolysis of complex metal-organic framework hybrids for oxygen reduction, *Adv. Funct. Mater.* 28 (2018) 1706738.
- S. Dou, X. Wang, S. Wang, Rational design of transition metal-based materials for highly efficient electrocatalysis, *Small Methods* 3 (2019) 1800211.
- H. Dai, B. Xia, L. Wen, C. Du, J. Su, W. Luo, G. Cheng, Synergistic catalysis of AgPd@ZIF-8 on dehydrogenation of formic acid, *Appl. Catal. B Environ.* 165 (2015) 57–62.
- H. Jin, H. Zhou, W. Li, Z. Wang, J. Yang, L. Chen, D. He, Y. Xiong, S. Mu, In situ derived Fe/N/S-Codoped carbon nanotubes from ZIF-8 crystals as efficient

- electrocatalysts for the oxygen reduction reaction and zinc-air batteries, *J. Mater. Chem. A* 6 (2018) 20093–20099.
- [32] Z. Wang, H. Jin, T. Meng, K. Liao, W. Meng, J. Yang, D. He, Y. Xiong, S. Mu, Fe, Cu-coordinated ZIF-derived carbon framework for efficient oxygen reduction reaction and zinc-air batteries, *Adv. Funct. Mater.* 28 (2018) 1802596.
- [33] S. Zhao, H. Yin, L. Du, L. He, K. Zhao, L. Chang, G. Yin, H. Zhao, S. Liu, Z. Tang, Carbonized nanoscale metal-organic frameworks as high performance electrocatalyst for oxygen reduction reaction, *ACS Nano* 8 (2014) 12660–12668.
- [34] S. Fu, C. Zhu, J. Song, D. Du, Y. Lin, Metal-organic framework-derived non-precious metal nanocatalysts for oxygen reduction reaction, *Adv. Energy Mater.* 7 (2017) 1700363.
- [35] P. Pachfule, D. Shinde, M. Majumder, Q. Xu, Fabrication of carbon nanorods and graphene nanoribbons from a metal-organic framework, *Nat. Chem.* 8 (2016) 718–724.
- [36] Q. Wei, X. Yang, G. Zhang, D. Wang, L. Zuin, D. Banham, L. Yang, S. Ye, Y. Wang, M. Mohamedi, S. Sun, An active and robust Si-Fe/N/C catalyst derived from waste reed for oxygen reduction, *Appl. Catal. B Environ.* 237 (2018) 85–93.
- [37] B. Li, H. Nam, J. Zhao, J. Chang, N. Lingappan, F. Yao, T. Lee, Y. Lee, Nanoreactor of nickel-containing carbon-shells as oxygen reduction catalyst, *Adv. Mater.* 29 (2017) 1605083.
- [38] M. Jiang, X. Cao, D. Zhu, Y. Duan, J. Zhang, Hierarchically porous N-doped carbon derived from ZIF-8 nanocomposites for electrochemical applications, *Electrochim. Acta* 196 (2016) 699–707.
- [39] R. Jiang, L. Li, T. Sheng, G. Hu, Y. Chen, L. Wang, Edge-site engineering of atomically dispersed Fe-N₄ by selective C-N bond cleavage for enhanced oxygen reduction reaction activities, *J. Am. Chem. Soc.* 140 (2018) 11594–11598.
- [40] E. Hu, X. Yu, F. Chen, Y. Wu, Y. Hu, X. Lou, Graphene layers-wrapped Fe/Fe₅C₂ nanoparticles supported on N-doped graphene nanosheets for highly efficient oxygen reduction, *Adv. Energy Mater.* 8 (2018) 1702476.
- [41] K. Yuan, S. Sfaelou, M. Qiu, D. Lützenkirchen-Hecht, X. Zhuang, Y. Chen, C. Yuan, X. Feng, U. ScherfK, Synergetic contribution of boron and Fe-Nx species in porous carbons toward efficient electrocatalysts for oxygen reduction reaction, *ACS Energy Lett.* 3 (2018) 252–260.
- [42] L. Jiao, G. Wan, R. Zhang, H. Zhou, S. Yu, H. Jiang, From metal-organic frameworks to single-atom Fe implanted N-doped porous carbons: efficient oxygen reduction in both alkaline and acidic media, *Angew. Chem. Int. Ed* 130 (2018) 8661–8665.
- [43] Z. Miao, X. Wang, M. Tsai, Q. Jin, J. Liang, F. Ma, T. Wang, S. Zheng, B. Hwang, Y. Huang, S. Guo, Q. Li, Atomically dispersed Fe-Nx/C electrocatalyst boosts oxygen catalysis via a new metal-organic polymer supramolecule strategy, *Adv. Energy Mater.* 8 (2018) 1801226.
- [44] Y. Wang, C. Zhu, S. Feng, Q. Shi, S. Fu, D. Du, Q. Zhang, Y. Lin, Interconnected Fe, S, N-Co doped hollow and porous carbon nanorods as efficient electrocatalysts for the oxygen reduction reaction, *ACS Appl. Mater. Inter.* 9 (2017) 40298–40306.
- [45] Q. Li, W. Chen, H. Xiao, Y. Gong, Z. Li, L. Zheng, X. Zheng, W. Yan, W. Cheong, R. Shen, N. Fu, L. Gu, Z. Zhuang, C. Chen, D. Wang, Q. Peng, J. Li, Y. Li, Fe isolated single atoms on S, N codoped carbon by copolymer pyrolysis strategy for highly efficient oxygen reduction reaction, *Adv. Mater.* 30 (2018) 1800588.
- [46] Y. Zhu, X. Chen, J. Liu, J. Zhang, D. Xu, W. Peng, Y. Li, G. Zhang, F. Zhang, X. Fan, Rational design of N-S-Fe-Doped nanoporous carbon catalysts from covalent triazine framework for high efficient ORR, *Chemsuschem* 11 (2018) 2402–2409.
- [47] Y. Qiu, J. Huo, F. Jia, B. Shanksa, W. Li, N- and S-doped mesoporous carbon as metal-free cathode catalysts for direct biorenewable alcohol fuel cells, *J. Mater. Chem. A* 4 (2016) 83–95.
- [48] Q. Wei, G. Zhang, X. Yang, Y. Fu, G. Yang, N. Chen, W. Chen, S. Sun, Litchi-like porous Fe/N/C spheres with atomically dispersed Fe-Nx promoted by sulfur as highly efficient oxygen electrocatalysts for Zn-Air batteries, *J. Mater. Chem. A* 6 (2018) 4605–4610.